

Photoinduced ferromagnetic and superconducting orders in multiorbital Hubbard models

Sujay Ray  and Philipp Werner 

Department of Physics, University of Fribourg, 1700 Fribourg, Switzerland

 (Received 12 March 2024; revised 6 June 2024; accepted 10 June 2024; published 8 July 2024)

The search for hidden orders in photoexcited lattice systems is an active research field driven by experimental reports of light-induced or light-stabilized phases. In this study, we investigate hidden electronic orders in strongly correlated two-orbital Hubbard models with orbital-dependent bandwidths. In equilibrium, the half-filled systems are antiferromagnetically ordered. Using nonequilibrium dynamical mean field theory we demonstrate the appearance of nonthermal ferromagnetic order in the photodoped state, if the two bandwidths are sufficiently different, and its coexistence with spin-singlet η superconductivity in the high photodoping region. Spin-triplet η -superconducting order appears instead if the two bandwidths are comparable. The rich nonequilibrium phasediagram uncovered in this work shows that Mott insulating multiorbital systems provide an interesting platform for the realization of nonthermal electronic orders.

DOI: [10.1103/PhysRevB.110.L041109](https://doi.org/10.1103/PhysRevB.110.L041109)

Introduction. The exploration of metastable or hidden phases, which cannot be accessed under equilibrium conditions, is an exciting research direction in condensed matter physics [1–6]. Due to the interplay between different active degrees of freedom [7], strongly correlated electron systems are particularly interesting candidates for the realization of such hidden phases [3,8–11]. Among them, Mott insulators have been shown to host different types of hidden phases [12–17] when excited by a laser pulse. Recent theoretical studies of photodoped Mott insulators identified nonthermal staggered superconducting (SC) orders in single-band and two-band Hubbard models [8,9,16–19], and chiral superconducting orders in geometrically frustrated systems [14]. Two-orbital Hubbard models have also been shown to exhibit nonthermal excitonic order [12] and Kugel-Khomskii spin-orbital order [15]. Because of the long lifetime of charge excitations in large-gap Mott insulators [20–23], a partial thermalization of charge carriers may occur in each Hubbard band, and these photodoped metastable states can be susceptible to new types of ordering instabilities. Due to the rapid advancement in laser technology, it becomes possible to induce and detect such metastable states [24,25], which also provides interesting perspectives for technological applications.

Several experimental and theoretical studies considered magnetic orders in photoexcited systems [10,24–34]. The phenomena range from ultrafast demagnetization [35,36] to magnetic switching and the appearance of nonthermal magnetic orders [15,26]. The double exchange model plays a prominent role in studies of photoinduced magnetic phases. In the context of perovskite manganites, a series of numerical investigations based on exact diagonalization and density matrix renormalization group calculations reported nonthermal magnetic phases [31–33,37–39]. However, these studies of closed systems lack a systematic control over the density and effective temperature of the photocarriers. While the nonthermal melting of Kugel-Khomskii spin-orbital order in a photodoped system has been investigated with nonequilibrium

dynamical mean field theory (DMFT) [15], the emergence of magnetic order is difficult to study in real-time simulations, due to heating effects and intrinsically slow dynamics.

Here we use the nonequilibrium steady state (NESS) approach [40], which provides a high level of control over the effective temperature and density of photocarriers, to study the two-orbital Hubbard model with orbital-dependent bandwidths. In large-gap Mott systems, this formalism is expected to give a qualitatively correct description of metastable photodoped states [41]. The interplay between more localized and more itinerant electrons leads to nontrivial couplings between the spin, orbital, and charge degrees of freedom and results in a multitude of hidden electronic orders.

Model and method. We consider the basic model for the investigation of multiorbital and Hund coupling effects, the two-orbital Hubbard model:

$$\begin{aligned}
 H = & - \sum_{\langle ij \rangle, \sigma} \sum_{\alpha=1,2} t_{\alpha}^{\text{hop}} c_{i,\alpha\sigma}^{\dagger} c_{j,\alpha\sigma} \\
 & + U \sum_i \sum_{\alpha=1,2} n_{i,\alpha\uparrow} n_{i,\alpha\downarrow} - \mu \sum_i \sum_{\alpha=1,2} (n_{i,\alpha\uparrow} + n_{i,\alpha\downarrow}) \\
 & + (U - 2J) \sum_{i,\sigma} n_{i,1\sigma} n_{i,2\bar{\sigma}} + (U - 3J) \sum_{i,\sigma} n_{i,1\sigma} n_{i,2\sigma},
 \end{aligned} \tag{1}$$

where $c_{i,\alpha\sigma}^{\dagger}$ ($c_{i,\alpha\sigma}$) is the creation (annihilation) operator at site i , α and σ denote the orbital and spin indices, respectively, t_{α}^{hop} is the orbital dependent nearest neighbor hopping amplitude between sites i and j , U is the intraorbital Hubbard repulsion, J the Hund coupling, and μ the chemical potential. In general, we assume different hopping parameters for the two orbitals and hence different bandwidths. We are interested in the strongly correlated regime of the half filled model, where both bands are Mott insulating, see the upper panel of Fig. 1.

In the NESS simulations [40], the system is weakly coupled to cold Fermion baths at each site. These baths induce charge carriers (triply and singly occupied sites) into our

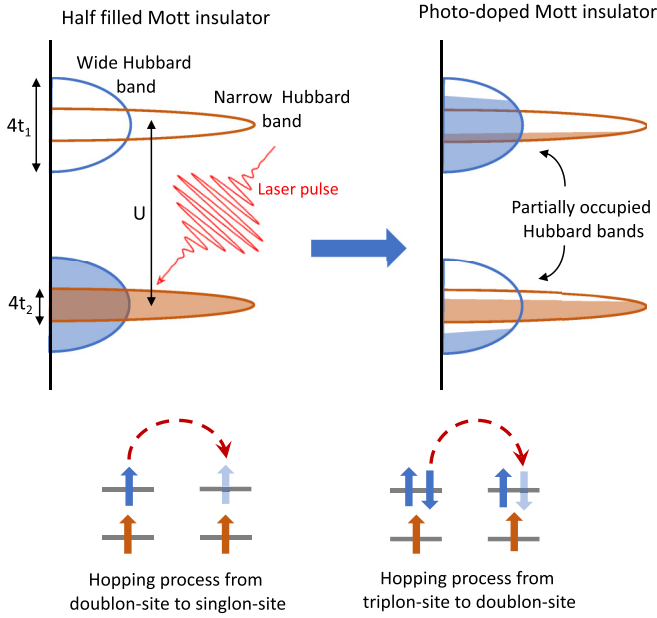


FIG. 1. Schematic diagram showing the photoexcitation in a two-orbital Mott insulator with different bandwidths. After the applied laser pulse, the wider band is photodoped more strongly than the narrower band. t_1^{hop} and t_2^{hop} are the hopping parameters for orbital 1 and 2, respectively. The bottom panels show the dominant hopping processes at holon/triplon density 0.25, which stabilize the FM state.

half-filled system, thus creating an effective photoexcited state. The Fermion baths are aligned with the lower and the upper Hubbard bands. The effective temperature of the photodoped carriers can be extracted by fitting a Fermi distribution function to the ratio of the occupied density of states and total density of states in the energy range of the Hubbard bands [16,17]. By choosing the chemical potential of the Fermion baths μ_b , we can control the density of photocarriers, while changing the temperature of the Fermion baths T_b allows to control their effective temperature. We can thus map out the nonequilibrium phase diagram of the photoexcited system as a function of photodoping concentration and effective temperature.

The DMFT simulations of the NESS are implemented for an infinitely connected Bethe lattice using the noncrossing approximation (NCA) as impurity solver [42,43]. The DMFT self-consistency equation in the Nambu-Keldysh formalism takes the form

$$\Delta(t, t') = t_0^2 \gamma G(t, t') \gamma + \sum_b D_b(t, t'). \quad (2)$$

Here Δ is the hybridization function, which has two contributions. The first term represents the lattice self-consistency for the Bethe lattice, with $t_0 = W/2$, where W is the half-bandwidth. The second term comes from the Fermionic baths and is defined in frequency space by $D_b(\omega) = g^2 \rho_b(\omega) = \Gamma \sqrt{W_b^2 - (\omega - \omega_b)^2}$, where $\Gamma = g^2/W_b^2$ is a dimensionless coupling constant, ω_b indicates the center of the energy spectrum, and W_b indicates the half-bandwidth of the bath b . In Eq. (5) we use the spinor basis $\psi^\dagger = (c_{1\uparrow}^\dagger \ c_{2\uparrow}^\dagger \ c_{1\downarrow} \ c_{2\downarrow})$ to study spin-singlet SC order and $\psi^\dagger = (c_{1\uparrow}^\dagger \ c_{2\uparrow}^\dagger \ c_{1\downarrow}^\dagger \ c_{2\downarrow})$ for

spin-triplet SC order. The choice of the spinor ψ^\dagger and the γ matrix allows us to study different magnetic and SC phases, see the Supplemental Material [44]. Because of the steady state assumption, the hybridization functions and Green's functions depend only on the time difference $t - t'$.

In all our calculations we use four fermion baths with $\omega_b = \pm U/2, \pm 3U/2$ and $W_b = 3.0$ and $\Gamma = 0.028$ for efficient photodoping, and we use the interaction parameters $U = 20$ and $J = 1$. The hopping parameter for orbital 1 is kept fixed at $t_1^{\text{hop}} = 1$, while t_2^{hop} for orbital 2 is varied from 0.1 to 1.0. We measure the photo-doping concentration by the triplon density, which we define as $\langle n_{1\uparrow} n_{1\downarrow} n_{2\uparrow} + n_{1\uparrow} n_{2\uparrow} n_{2\downarrow} - 4n_{1\uparrow} n_{1\downarrow} n_{2\uparrow} n_{2\downarrow} \rangle$, with $n_\alpha = n_{\alpha\uparrow} + n_{\alpha\downarrow}$ the occupation of orbital α . In addition, we define the magnetic orders via the local magnetization $m_i = \sum_\alpha n_{i,\alpha\uparrow} - n_{i,\alpha\downarrow}$, and two types of SC order—spin-singlet orbital-triplet order $p_{i,oy} = \frac{1}{4} \sum_\alpha (c_{i,\alpha\uparrow}^\dagger c_{i,\alpha\downarrow}^\dagger + \text{H.c.})$, and spin-triplet orbital-singlet SC order $p_{i,sy} = \frac{1}{4} \sum_\sigma (c_{i,1\sigma}^\dagger c_{i,2\sigma}^\dagger + \text{H.c.})$. In a staggered SC state (η order) or staggered antiferromagnetic state (AFM order) these order parameters have opposite signs on the two sublattices A and B ,

$$\eta_{i,oy(sy)}^x = \delta_i^{A/B} p_{i,oy(sy)}, \quad (3)$$

$$M_{i,AFM} = \delta_i^{A/B} m_i, \quad (4)$$

with $\delta_i^{A(B)} = 1 (-1)$ for i on the $A (B)$ sublattice.

In order to study different phases we apply small seed fields which couple to the order parameters of interest. In a symmetry-broken state the order parameter grows to a high value and becomes almost independent of the value of the seed field. In the DMFT calculations, we switch off the seed field after some iterations, so that the symmetry-broken phase can be unambiguously identified by a nonzero order parameter. We cannot simultaneously realize $\eta_{i,oy}^x$ and $\eta_{i,sy}^x$ SC orders, since they correspond to different ψ^\dagger and γ , while FM and $\eta_{i,oy}^x$ order can be simultaneously stabilized.

Photoinduced hidden orders. We first study the nonequilibrium phase diagram as a function of photodoping (triplon density) and the hopping parameter of the narrow band (t_2^{hop}), see Fig. 2. To probe the ferromagnetic (FM) and spin-singlet η -SC states, we add the seed terms $H_{\text{seed}} = B_{\text{seed}} \sum_i m_i + P_{\text{seed}} \sum_i (c_{i,1\uparrow}^\dagger c_{i,1\downarrow}^\dagger + c_{i,2\uparrow}^\dagger c_{i,2\downarrow}^\dagger + \text{H.c.})$ to our Hamiltonian (1), where B_{seed} and P_{seed} are, respectively, small magnetic and superconducting seed fields. Due to the partial thermalization of the electrons in each Hubbard band, the photodoped state can be represented by an equilibrium state with a fixed number of multiplets (triplons, doublons, and singlons), described by the effective low energy model [17,46]

$$H_{\text{eff}} = H_{\text{hop}}(P_{in}P_{jn-1}) + H_{s/o}(P_{in}P_{jn}) + H_\eta(P_{in}P_{jn-2}), \quad (5)$$

where P_{in} is the projection operator at site i on states with particle number n . The first term in Eq. (5) is the hopping term $-\sum_{\langle ij \rangle} \sum_{\alpha\sigma} t_\alpha^{\text{hop}} c_{i,\alpha\sigma}^\dagger c_{j,\alpha\sigma}$ which acts on sites which differ in particle number by one. The second term is the spin-orbital term $2(t_\alpha^{\text{hop}})^2/U \sum_{\langle ij \rangle} (\frac{1}{2} + 2s_i \cdot s_j)(\frac{1}{2} + 2\tau_i \cdot \tau_j)$ and acts on sites with the same particle numbers, where s_i and τ_i are spin and orbital pseudospin operators at site i . Hund coupling $J > 0$ ($J < 0$) favors spin (orbital) order. The last term is

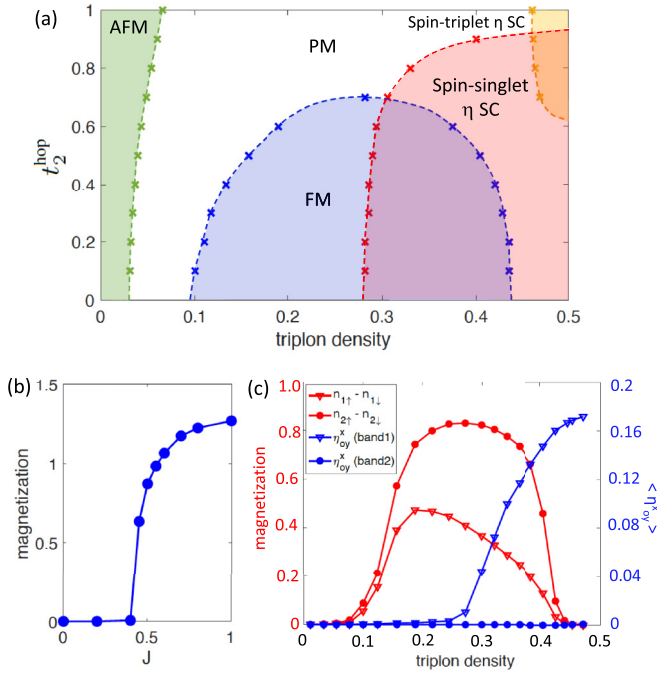


FIG. 2. (a) Nonequilibrium phase diagram of the photodoped half-filled two-orbital Hubbard model with different bandwidths ($U = 20, J = 1$) as a function of the triplon density and hopping parameter t_2^{hop} of the narrow band ($t_1^{\text{hop}} = 1$). AFM order (an extension of the equilibrium phase) appears for small triplon density, whereas a FM state is stabilized for intermediate photodoping and low t_2^{hop} . For higher photodoping, a spin-singlet η -SC order is stabilized for smaller values of t_2^{hop} and spin-triplet η -SC appears for very strong photodoping when $t_2^{\text{hop}} \sim t_1^{\text{hop}}$. (b) FM order parameter as a function of Hund coupling J at triplon density 0.27 for $t_2^{\text{hop}} = 0.3$. The vanishing magnetization at small J shows the role of Hund coupling in stabilizing the FM state. (c) Magnetization and η_{xy}^s order in band 1 and band 2 for $t_2^{\text{hop}} = 0.3$. The magnetization is dominated by band 2, while the η -SC order is hosted by band 1. The effective temperature in all calculations is kept at $\beta_{\text{eff}} \sim 55$.

the η -pseudospin term given by $-4(t_\alpha^{\text{hop}})^2/U \sum_{(ij),\nu} (\eta_{iv}^+ \eta_{jv}^- + \eta_{iv}^- \eta_{jv}^+)$ with ν an index for the six different SC orders (three spin-singlet orbital-triplet and three spin-triplet orbital-singlet orders, see the Supplemental Material [44]). This term acts on sites which differ in particle number by two [17].

Near zero photodoping, there are negligible charge excitations and the system is governed by the $H_{s/o}$ term, which stabilizes the antiferromagnetic (AFM) phase with a transition temperature (T_c) of the order of $(t_\alpha^{\text{hop}})^2/U$. As the photodoping is increased, the diffusing charge carriers melt the AFM phase, which results in a nonthermal PM metal. As the bandwidth of the narrower band (t_2^{hop}) is decreased, the T_c also decreases, since we are on the strongly correlated side of the AFM dome. This shifts the boundary between the AFM and PM phases toward lower photodoping. At intermediate photodoping, the hopping term H_{hop} starts to dominate, because of the substantial density of singly occupied (singlon), doubly occupied (doublon), and triply occupied (triplon) sites. If we decrease t_2^{hop} in this regime to localize the electrons in the narrower band, a nonthermal FM state is stabilized

by the interplay of Hund coupling and kinetic energy. A positive Hund coupling J favors high-spin doublon states. On the other hand, the hopping processes in the wide band from doublon to singlon and from triplon to doublon sites, illustrated in the bottom panel of Fig. 1, stabilize the FM state since this state allows to gain kinetic energy while keeping the local spin arrangement unchanged. Any other hopping processes would create a configuration with higher energy. Thus, a nonthermal FM phase appears at lower t_2^{hop} values and near triplon/singlon density 0.25 for $J > 0$. In the absence of Hund coupling, all the local doublon states are degenerate in energy and the hopping term is not expected to favor the FM state. Indeed, by decreasing the Hund coupling, the FM magnetization disappears below a critical value of J , as shown in Fig. 2(b).

When the photodoping is increased further, more charge excitations are created and for $t_1^{\text{hop}} = t_2^{\text{hop}} = 1$, in the high doping limit (triplon density $\gtrsim 0.46$) spin-triplet orbital-singlet η -SC order (η_{sy}^x) develops [17]. As shown in Fig. 2(a), this order disappears when t_2^{hop} is decreased. For small t_2^{hop} , the charge excitations are mostly concentrated in the wider band, while the narrower band remains close to half-filled (e.g., for $t_1^{\text{hop}} = 1, t_2^{\text{hop}} = 0.3$, triplon density ~ 0.28 and $\beta_{\text{eff}} \sim 55$, the double occupancies in the wider band and the narrower band are 0.25 and 0.03, respectively). At sufficiently low effective temperature, the doublons and singlons in the wide band condense to give rise to spin-singlet orbital-triplet η_{oy} order. Since the dominant contribution to the η_{oy} order comes from the wider band ($c_{i,1\uparrow}^\dagger c_{i,1\downarrow}^\dagger$), we have an orbital selective η_{oy} order [see Fig. 2(c)].

Interestingly, in the photodoping region with triplon density between 0.3 and 0.4, both the first and last term in Eq. (5) contribute and we find a coexistence of FM and η -SC order. At first sight, this is surprising, since magnetic order is usually detrimental to singlet pairing. Here, such a coexistence is possible because the two photoinduced order parameters are supported by different orbitals—the wider band hosts the SC order, while the FM order is dominated by the spin-aligned localized electrons in the narrower band, as shown in Fig. 2(c).

Next, we fix $t_1^{\text{hop}} = 1, t_2^{\text{hop}} = 0.4$ and investigate the phase diagram in the space of triplon density and inverse effective temperature β_{eff} , see Fig. 3. At low T_{eff} (high $\beta_{\text{eff}} \sim 50$), we have AFM order at low photodoping. Around triplon density 0.25 the FM phase appears, while at large photodoping, we find the η_{oy} -SC phase, which partly coexists with the FM phase. With increasing temperature (decreasing β_{eff}) the ordered regions shrink and they disappear at similar T_c values. The highest effective T_c for the nonthermal FM order is around triplon density ~ 0.29 , which is consistent with the optimal doping deduced from the phase diagram in Fig. 2(a). The η_{oy} phase shows a similar temperature dependence as in the one band Hubbard model [16], consistent with our observation that the η_{oy} -SC state is essentially decoupled from the narrow band and has single-band characteristics.

We see from Fig. 3 that both the nonthermal FM and η -SC orders appear at $\beta_{\text{eff}} > 30$. While this is a high temperature for realistic parameters, it is difficult to realize these effective temperatures in real-time simulations of a photoexcited multi-orbital system, and presumably also in experiments, even

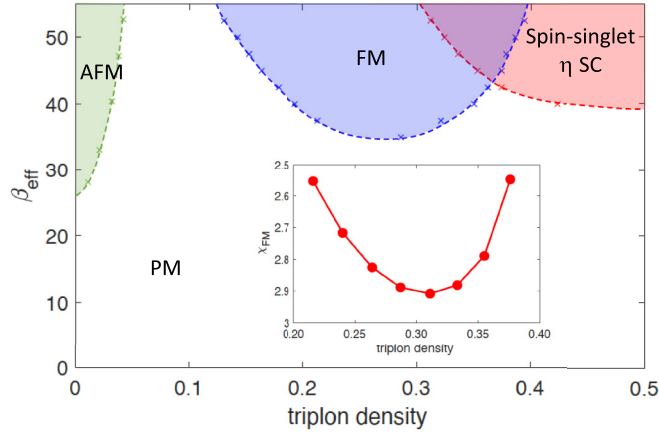


FIG. 3. NESS phase diagram of the two-orbital Hubbard model with $U = 20$, $J = 1$, $t_1^{\text{hop}} = 1$, and $t_2^{\text{hop}} = 0.4$ in the space of β_{eff} and triplon density. The AFM phase appears in the undoped and weakly photodoped region, while the η SC state is stabilized in the high photodoping region. At intermediate photodoping we have the FM state. In these simulations, T_b is varied to achieve different β_{eff} . The inset of the figure shows the FM susceptibility χ_{FM} , estimated from the real-time calculations, as a function of doping. The optimal doping condition for FM order is consistent in both calculations.

using the entropy cooling technique [47]. However, near the optimal photodoping density, we still expect to find an enhanced FM susceptibility at the accessible higher T_{eff} .

Real-time simulations. To investigate the dynamics and measure the magnetic susceptibilities, we employ the entropy cooling technique [47,48] to minimize the heating effect in nonequilibrium photodoped Mott insulators. In this setup, we start with a half-filled Mott insulating state and add two additional narrow noninteracting Fermion baths (one completely full and one completely empty) as shown in Fig. 4(a). These baths are coupled to the Mott insulating system by a hopping term v_{sb} . To facilitate an efficient photodoping, while keeping the effective temperature of the system low, the hopping term is modulated in time as $v_{sb}(t) = A_0 f_{\text{en}}(t) \sin(\Omega(t)t)$, where $A_0 = 1$ denotes the amplitude of the hopping, $f_{\text{en}}(t)$ is an envelope function determining the switch-on and switch-off times of the hopping, and $\Omega(t)$ is a time-dependent (chirped) frequency. In our calculations for the $U = 20$, $J = 1$ model, we chose $f_{\text{en}}(t) = \exp(-((t - t_c)/2\sigma)^2)$ as a Gaussian with $t_c = 12$, and $\sigma = 2.8$. $\Omega(t)$ is increased linearly from an initial value $\Omega_{\text{ini}} = 27.0$ to a final value $\Omega_{\text{fin}} = 29.8$. The hopping modulation pulse is shown in Fig. 4(c) (yellow curve). In this setup, the DMFT self-consistency condition becomes

$$\Delta(t, t') = t_0(t)^2 \gamma G(t, t') \gamma + \sum_{\alpha} v_{sb}(t)^2 G_{\text{bath},\alpha}(t, t'), \quad (6)$$

where $t_0(t) = t_0$ is kept fixed, $G(t, t')$ is the Green's function of the system, and $G_{\text{bath},\alpha}(t, t')$ is the Green's function of the noninteracting bath with flavor α (full, empty).

Because of the conservation of total spin in our Hamiltonian, it is not possible to simulate the switching to a purely FM state within this framework. Thus, in order to study the photoinduced FM state, we implemented a four-impurity calculation, which mimics the bilayer system shown in Fig. 4(b).

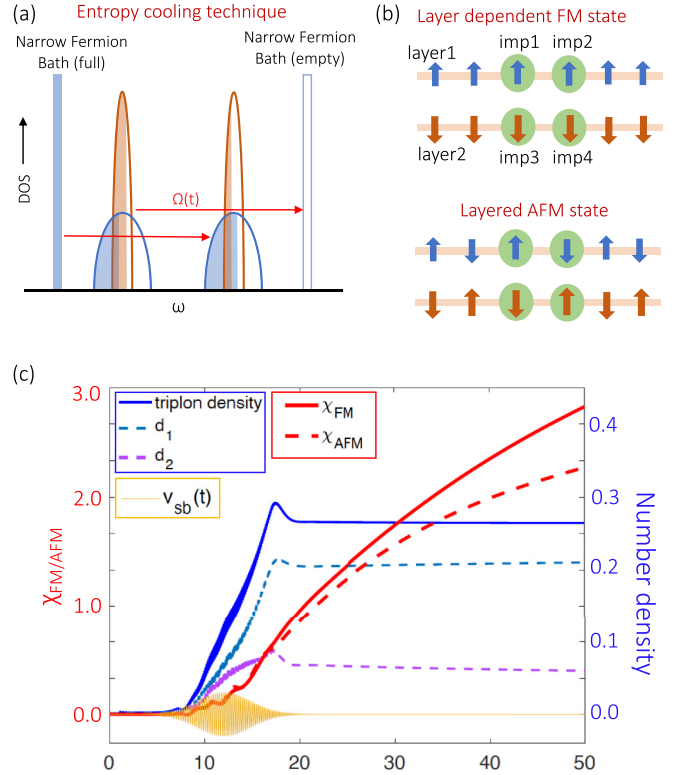


FIG. 4. (a) Illustration of the entropy cooling technique, where electrons are injected into the upper Hubbard bands from a fully occupied narrow Fermion bath and electrons are ejected from the lower Hubbard bands to an empty Fermion bath. (b) Schematic diagram of the four-impurity DMFT calculation mimicking the dynamics in two bilayer systems—an AFM system (bottom) and an AFM stacked FM system (top). (c) Magnetic susceptibility $\chi_{\text{FM/AFM}}$ in the FM and AFM state (red curves) and time evolution of various local observables—triplon density (blue solid), double occupancy in orbital 1 (d_1) and orbital 2 (d_2). The yellow curve shows the hopping pulse $v_{sb}(t)$ (not to scale) used to produce the photodoping.

Here, the impurity models 1 and 2 represent two neighboring sites in layer 1, whereas the impurity models 3 and 4 represent the corresponding sites in layer 2. In this setup, an AFM state is identified by AFM spin alignments in all four pairs of neighboring impurities, while a FM state is indicated by a layer-dependent magnetization, e.g., with spin-up polarization on impurities 1 and 2 and spin-down polarization on impurities 3 and 4 [see Fig. 4(b)].

In Fig. 4(c) we show the result of the real-time DMFT calculation. As soon as the coupling to the narrow baths is switched on, the system gets photodoped, as indicated by the increasing triplon density during the pulse. As a result of the different bandwidths, the double occupancy in orbital 1 (d_1) grows larger than in orbital 2 (d_2), which is consistent with the results of the NESS calculations. The magnetic susceptibility is measured by dividing the magnetization (magnetic order parameter) by the corresponding seed field as $\chi = \langle m \rangle / B_{\text{seed}}$. In Fig. 4(c), we show the χ_{FM} and χ_{AFM} estimates for FM and AFM order. In the FM case, we choose $B_{\text{seed}} > 0$ for impurity 1 and 2, $B_{\text{seed}} < 0$ for impurity 3 and 4, while in the AFM case $B_{\text{seed}} > 0$ for impurity 1 and 4 and $B_{\text{seed}} < 0$

for impurity 2 and 3. The FM susceptibility grows larger than the AFM one and keeps increasing at the longest simulation times, indicating a dominant tendency toward FM ordering. We can also control the photodoping concentration through the final frequency Ω_{fin} of the chirped pulse and extract χ_{FM} as a function of the triplon density, as shown in the inset of Fig. 3. We find that χ_{FM} reaches a maximum value near triplon density ~ 0.3 , which agrees with the optimal photodoping concentration for the FM phase in the NESS simulations. We note that for bandwidths of the order of eV, our unit of time is of the order of fs. The real-time simulations, which represent the dynamics of a laser-excited system, thus show that with optimized pulse shapes, a significant enhancement of the FM susceptibility can be achieved on a sub-ps timescale.

Conclusions. We demonstrated that the photodoped two-band Hubbard model with orbital-dependent bandwidths hosts nonthermal FM and staggered SC order, and even a coexistence of both orders. Cold atom systems, in which a long lifetime of “photocarriers” can be achieved [20,21], and for which the implementation of multiorbital physics has recently been proposed [49], are an interesting platform for experimental realizations. Manganites, which are often described by the

double exchange model, and NiO, with two Mott insulating half-filled e_g bands, an interaction to bandwidth ratio $U/W \approx 5$ and $J/U \approx 1/10$ [50], are possible candidates for the observation of these nonthermal electronic orders in real materials. While it is challenging to realize sufficiently cold photodoped states for symmetry breaking, the use of entropy cooling protocols [47,51] and optimized chirped pulses [48] should allow to induce photodoped transient states with enhanced susceptibilities for the nonthermal orders. In connection with light-induced superconductivity and the transient Meissner effect, novel techniques for measuring ultrafast changes in magnetization and magnetic susceptibilities are being developed [52]. These techniques will enable experimental tests of our predictions for light-induced ferromagnetism and η pairing.

Acknowledgments. We thank Y. Murakami for helpful comments on the manuscript and the Swiss National Science Foundation for the funding (Grant No. 200021-196966). The nonequilibrium DMFT calculations are based on the NESSi library [53] and the NESS simulations on a code originally developed by J. Li and M. Eckstein. The calculations were run on the beo06 cluster at the University of Fribourg.

-
- [1] H. Ichikawa, S. Nozawa, T. Sato, A. Tomita, K. Ichiyanagi, M. Chollet, L. Guerin, N. Dean, A. Cavalleri, S.-i. Adachi *et al.*, Transient photoinduced hidden phase in a manganite, *Nat. Mater.* **10**, 101 (2011).
- [2] L. Stojchevska, I. Vaskivskiy, T. Mertelj, P. Kusar, D. Svetin, S. Brazovskii, and D. Mihailovic, Ultrafast switching to a stable hidden quantum state in an electronic crystal, *Science* **344**, 177 (2014).
- [3] D. Fausti, R. I. Tobey, N. Dean, S. Kaiser, A. Dienst, M. C. Hoffmann, S. Pyon, T. Takayama, H. Takagi, and A. Cavalleri, Light-induced superconductivity in a stripe-ordered cuprate, *Science* **331**, 189 (2011).
- [4] A. Cavalleri, Photo-induced superconductivity, *Contemp. Phys.* **59**, 31 (2018).
- [5] A. de la Torre, D. M. Kennes, M. Claassen, S. Gerber, J. W. McIver, and M. A. Sentef, *Colloquium: Nonthermal pathways to ultrafast control in quantum materials*, *Rev. Mod. Phys.* **93**, 041002 (2021).
- [6] Y. Murakami, D. Golež, M. Eckstein, P. Werner, Photo-induced nonequilibrium states in Mott insulators, *arXiv:2310.05201*.
- [7] E. Dagotto, Complexity in strongly correlated electronic systems, *Science* **309**, 257 (2005).
- [8] Y. Murakami, S. Takayoshi, T. Kaneko, A. M. Läuchli, and P. Werner, Spin, charge, and η -spin separation in one-dimensional photodoped Mott insulators, *Phys. Rev. Lett.* **130**, 106501 (2023).
- [9] Y. Murakami, S. Takayoshi, T. Kaneko, Z. Sun, D. Gole, A. J. Millis, and P. Werner, Exploring nonequilibrium phases of photo-doped Mott insulators with generalized Gibbs ensembles, *Commun. Phys.* **5**, 23 (2022).
- [10] A. Kirilyuk, A. V. Kimel, and T. Rasing, Ultrafast optical manipulation of magnetic order, *Rev. Mod. Phys.* **82**, 2731 (2010).
- [11] M. Mitranò, A. Cantaluppi, D. Nicoletti, S. Kaiser, A. Perucchi, S. Lupi, P. Di Pietro, D. Pontiroli, M. Ricco, S. R. Clark *et al.*, Possible light-induced superconductivity in K_3C_{60} at high temperature, *Nature (London)* **530**, 461 (2016).
- [12] P. Werner, and Y. Murakami, Nonthermal excitonic condensation near a spin-state transition, *Phys. Rev. B* **102**, 241103(R) (2020).
- [13] R. Mikhaylovskiy, E. Hendry, A. Secchi, J. H. Mentink, M. Eckstein, A. Wu, R. Pisarev, V. Kruglyak, M. Katsnelson, T. Rasing *et al.*, Ultrafast optical modification of exchange interactions in iron oxides, *Nat. Commun.* **6**, 8190 (2015).
- [14] J. Li, M. Müller, A. Kim, A. Läuchli, and P. Werner, Twisted chiral superconductivity in photodoped frustrated Mott insulators, *Phys. Rev. B* **107**, 205115 (2023).
- [15] J. Li, H. U. R. Strand, P. Werner and M. Eckstein, Ultrafast coupled charge and spin dynamics in strongly correlated NiO, *Nat. Commun.* **9**, 4581 (2018).
- [16] J. Li, D. Golez, P. Werner, and M. Eckstein, η -paired superconducting hidden phase in photodoped Mott insulators, *Phys. Rev. B* **102**, 165136 (2020).
- [17] S. Ray, Y. Murakami, and P. Werner, Nonthermal superconductivity in photodoped multiorbital Hubbard systems, *Phys. Rev. B* **108**, 174515 (2023).
- [18] S. Ejima, T. Kaneko, F. Lange, S. Yunoki, and H. Fehske, Photoinduced η -pairing at finite temperatures, *Phys. Rev. Res.* **2**, 032008(R) (2020).
- [19] T. Kaneko, S. Yunoki, and A. J. Millis, Charge stiffness and long-range correlation in the optically induced η -pairing state of the one-dimensional Hubbard model, *Phys. Rev. Res.* **2**, 032027(R) (2020).
- [20] N. Strohmaier, D. Greif, R. Jördens, L. Tarruell, H. Moritz, T. Esslinger, R. Sensarma, D. Pekker, E. Altman, and E. Demler,

- Observation of elastic doublon decay in the Fermi-Hubbard model, *Phys. Rev. Lett.* **104**, 080401 (2010).
- [21] R. Sensarma, D. Pekker, E. Altman, E. Demler, N. Strohmaier, D. Greif, R. Jördens, L. Tarruell, H. Moritz, and T. Esslinger, Lifetime of double occupancies in the Fermi-Hubbard model, *Phys. Rev. B* **82**, 224302 (2010).
- [22] M. Eckstein and P. Werner, Thermalization of a pump-excited Mott insulator, *Phys. Rev. B* **84**, 035122 (2011).
- [23] Z. Lenarčič and P. Prelovsec, Charge recombination in undoped cuprates, *Phys. Rev. B* **90**, 235136 (2014).
- [24] A. Cavalleri, C. Toth, C. W. Siders, J. A. Squier, F. Raksi, P. Forget, and J. C. Kieffer, Femtosecond structural dynamics in VO₂ during an ultrafast solid-solid phase transition, *Phys. Rev. Lett.* **87**, 237401 (2001).
- [25] E. Collet, M. H. Lemée-Cailleau, M. Le Cointe, H. Cailleau, M. Wulff, T. Luty, S. Koshihara, M. Meyer, L. Toupet, P. Rabiller, and S. Teichert, Laser-induced ferroelectric structural order in an organic charge-transfer crystal, *Science* **300**, 612 (2003).
- [26] T. Li, A. Patz, L. Mouchliadis, J. Yan, T. A. Lograsso, I. E. Perakis, and J. Wang, Femtosecond switching of magnetism via strongly correlated spincharge quantum excitations, *Nature (London)* **496**, 69 (2013).
- [27] S. Wall, D. Brida, S. R. Clark, H. P. Ehrke, D. Jaksch, A. Ardavan, S. Bonora, H. Uemura, Y. Takahashi, T. Hasegawa, H. Okamoto, G. Cerullo, and A. Cavalleri, Quantum interference between charge excitation paths in a solid-state Mott insulator, *Nat. Phys.* **7**, 114 (2011).
- [28] J. H. Mentink, Manipulating magnetism by ultrafast control of the exchange interaction, *J. Phys.: Condens. Matter* **29**, 453001 (2017).
- [29] H. Matsueda and S. Ishihara, Photoinduced charge and spin dynamics in strongly correlated electron systems, *J. Phys. Soc. Jpn.* **76**, 083703 (2007).
- [30] Y. Kanamori, H. Matsueda, and S. Ishihara, Photoinduced change in the spin state of itinerant correlated electron systems, *Phys. Rev. Lett.* **107**, 167403 (2011).
- [31] Y. Kanamori, H. Matsueda, and S. Ishihara, Dynamical coupling and separation of multiple degrees of freedom in a photoexcited double-exchange system, *Phys. Rev. Lett.* **103**, 267401 (2009).
- [32] Y. Kanamori, H. Matsueda, and S. Ishihara, Numerical study of photoinduced dynamics in a double-exchange model, *Phys. Rev. B* **82**, 115101 (2010).
- [33] K. Miyano, T. Tanaka, Y. Tomioka, and Y. Tokura, Photoinduced insulator-to-metal transition in a perovskite manganite, *Phys. Rev. Lett.* **78**, 4257 (1997).
- [34] W. Koshibae, N. Furukawa, and N. Nagaosa, Real-time quantum dynamics of interacting electrons: Self-organized nanoscale structure in a spin-electron coupled system, *Phys. Rev. Lett.* **103**, 266402 (2009).
- [35] E. Beaurepaire, J. C. Merle, A. Daunois, and J. Y. Bigot, Ultrafast spin dynamics in ferromagnetic nickel, *Phys. Rev. Lett.* **76**, 4250 (1996).
- [36] B. Koopmans, G. Malinowski, F. Dalla Longa, D. Steiauf, M. Fähnle, T. Roth, M. Cinchetti, and M. Aeschlimann, Explaining the paradoxical diversity of ultrafast laser-induced demagnetization, *Nat. Mater.* **9**, 259 (2010).
- [37] M. Fiebig, K. Miyano, Y. Tomioka, Y. Tokura, Visualization of the local insulator-metal transition in Pr_{0.7}Ca_{0.3}MnO₃, *Science* **280**, 1925 (1998).
- [38] R. D. Averitt, A. I. Lobad, C. Kwon, S. A. Trugman, V. K. Thorsmolle, and A. J. Taylor, Ultrafast conductivity dynamics in colossal magnetoresistance manganites, *Phys. Rev. Lett.* **87**, 017401 (2001).
- [39] A. Ono, S. Ishihara, Photocontrol of magnetic structure in an itinerant magnet, *Phys. Rev. B* **98**, 214408 (2018).
- [40] J. Li and M. Eckstein, Nonequilibrium steady-state theory of photodoped Mott insulators, *Phys. Rev. B* **103**, 045133 (2021).
- [41] F. Künzel, A. Erpenbeck, D. Werner, E. Arrigoni, E. Gull, G. Cohen, and M. Eckstein, Numerically exact simulation of photodoped Mott insulators, *Phys. Rev. Lett.* **132**, 176501 (2024).
- [42] H. Keiter and J. C. Kimball, Perturbation technique for the Anderson Hamiltonian, *Phys. Rev. Lett.* **25**, 672 (1970).
- [43] M. Eckstein and P. Werner, Nonequilibrium dynamical mean-field calculations based on the noncrossing approximation and its generalizations, *Phys. Rev. B* **82**, 115115 (2010).
- [44] See Supplemental Material at <http://link.aps.org/supplemental/10.1103/PhysRevB.110.L041109> for a detailed description of the effective low energy model in Eq. (5) and details of DMFT calculations, and a description of the method used to determine the phase boundaries in Figs. 2(a) and 3. It also contains Ref. [45].
- [45] S. Hoshino and P. Werner, Electronic orders in multiorbital Hubbard models with lifted orbital degeneracy, *Phys. Rev. B* **93**, 155161 (2016).
- [46] S.-S. B. Lee, J. v. Delft, and A. Weichselbaum, Generalized Schrieffer-Wolff transformation of multiflavor Hubbard models, *Phys. Rev. B* **96**, 245106 (2017).
- [47] P. Werner, M. Eckstein, M. Müller, and G. Refael, Light-induced evaporative cooling of holes in the Hubbard model, *Nat. Commun.* **10**, 5556 (2019).
- [48] P. Werner, J. Li, D. Golez, and M. Eckstein, Entropy-cooled nonequilibrium states of the Hubbard model, *Phys. Rev. B* **100**, 155130 (2019).
- [49] A. Richaud, M. Ferraretto, and M. Capone, Mimicking multi-orbital systems with SU(N) atoms: Hund's physics and beyond, *Condensed Matter* **7**, 18 (2022).
- [50] L. Zhang, P. Staar, A. Kozhevnikov, Y.-P. Wang, J. Trinastic, T. Schulthess, and H.-P. Cheng, DFT+DMFT calculations of the complex band and tunneling behavior for the transition metal monoxides MnO, FeO, CoO, and NiO, *Phys. Rev. B* **100**, 035104 (2019).
- [51] J. S. Bernier, C. Kollath, A. Georges, L. De Leo, F. Gerbier, C. Salomon, and C. Köhl, Cooling fermionic atoms in optical lattices by shaping the confinement, *Phys. Rev. A* **79**, 061601(R) (2009).
- [52] S. Fava, G. De Vecchi, G. Jotzu, M. Buzzi, T. Gebert, Y. Liu, B. Keimer, and A. Cavalleri, Magnetic field expulsion in optically driven YBa₂Cu₃O_{6.48}, [arXiv:2405.00848](https://arxiv.org/abs/2405.00848).
- [53] M. Schüler, D. Golelez, Y. Murakami, N. Bittner, A. Herrmann, H. U. R. Strand, P. Werner, and M. Eckstein, NESSi: The non-equilibrium systems simulation package, *Comput. Phys. Commun.* **257**, 107484 (2020).